INTERNATIONAL SOCIETY FOR
SOIL MECHANICS AND
GEOTECHNICAL ENGINEERING

This paper was downloaded from the Online Library of the International Society for Soil Mechanics and Geotechnical Engineering (ISSMGE). The library is available here:

https://www.issmge.org/publications/online-library

This is an open-access database that archives thousands of papers published under the Auspices of the ISSMGE.

The paper was published in the proceedings of the 11th International Conference on Physical Modelling in Geotechnics (ICPMG2026) and was edited by Ioannis Anastasopoulos. The conference was held from June 8th to June 12th 2026 in Zurich, Switzerland.

Proceedings of the 11th ICPMG 2026
11th International Conference on Physical Modelling in Geotechnics
8-12 June 2026, Zurich, Switzerland
© 2026 the Authors

Towards fibre optic shape sensing for geotechnical model testing

Qiru Yang
The University of Melbourne, Melbourne, Australia, qiruy@student.unimelb.edu.au

Yifa Wang, Mahdi M. Disfani
The University of Melbourne, Melbourne, Australia, yifa.wang@unimelb.edu.au, mahdi.miri@unimelb.edu.au

Xiaomin Xu
The University of Manchester, Manchester, UK, The University of Cambridge, Cambridge, UK, xiaomin.xu@manchester.ac.uk

Mark J. Cassidy, Yinghui Tian
The University of Melbourne, Melbourne, Australia, mark.cassidy@unimelb.edu.au, yinghui.tian@unimelb.edu.au

ABSTRACT: Fibre optic shape sensing is well established in medical and aerospace applications, yet its adoption in geotechnical engineering remains limited. In physical modelling, accurate measurement of continuous structural shape is critical for advancing understanding of soil-structure interaction, while conventional techniques are typically restricted to discrete measurements or require direct visual access. Fibre optic shape sensing provides a distributed, real-time, and minimally invasive means of reconstructing internal structural shape within the soil mass, with potential applications to tunnels, pipelines, and mooring or anchor lines. This study experimentally investigates Fibre Bragg Grating (FBG)-based shape sensing using single-fibre and multi-fibre sensor configurations. Shape reconstruction is performed by converting distributed strain measurements into curvature and global shape profiles. A cantilever aluminium plate instrumented with a three-fibre sensor is tested under controlled loading to evaluate reconstruction accuracy. The performance of single-fibre and multi-fibre shape sensing algorithms is systematically compared to assess their accuracy, robustness, and applicability. The results demonstrate that FBG-based shape sensing can achieve accurate and reliable shape reconstruction, highlighting its strong potential for use in scaled geotechnical model testing.

1 INTRODUCTION

Physical model testing, including 1*g* laboratory tests and geotechnical centrifuge modelling, plays a crucial role in advancing the understanding of soil-structure interaction in geotechnical engineering. Such methods have been widely applied to study the behaviour of geostructures such as piles, retaining walls, and tunnels (Wood, 2017). In these experiments, accurately capturing the continuous shape evolution of embedded structural elements is essential, particularly in situations where direct visual access is not possible.

Conventional shape sensing techniques suffer from several inherent limitations. Discrete sensors, such as strain gauges, require intrusive installation and extensive wiring, potentially disturbing the local stress field and failing to capture localised or highly non-uniform deformations (Barrias et al., 2016). Non-intrusive optical techniques, such as Particle Image Velocimetry (PIV), have significantly advanced the measurement of soil kinematics by tracking particle displacements between successive images (Stanier et al., 2016; White et al., 2003). Although PIV is highly effective for monitoring surface deformation, its applicability to embedded structures within opaque soil masses is limited. Measurements are typically restricted to transparent boundaries and in-plane motion, which constrains the ability to resolve three-dimensional or out-of-plane deformation within the soil mass (Raffel et al., 2018). These limitations highlight the need for a distributed sensor that can be embedded directly within structural elements, enabling continuous shape sensing without compromising mechanical interaction with the surrounding soil.

Fibre Optic Shape Sensing (FOSS) has emerged as a powerful technique for distributed measurement and high-precision shape reconstruction. It has been widely adopted in fields that require accurate shape tracking, such as aerospace engineering for monitoring wing deformation, and medical robotics for tracking instruments including needles and catheters. However, its application in geotechnical shape sensing remains limited due to factors such as optic fibre fragility, integration challenges, and the lack of validated implementation frameworks for soil-structure interaction problems (Zhang et al., 2019). FOSS enables dynamic and direct tracking of structural shapes while offering mechanical flexibility, embedment capability, and independence from visual access (Floris et al., 2021). Additionally, its high sensitivity, flexibility and resistance to harsh environments make FOSS particularly attractive for geotechnical model testing and field monitoring applications.

From an interrogation perspective, FOSS can be broadly classified into distributed and quasi-distributed (grating-based) sensing systems (Di Sante, 2015). Distributed Fibre Optic Sensors (DFOS) provide continuous strain measurements along the fire length. However, their relatively low spatial resolution limits high positional accuracy. As a result, most DFOS applications have focused on strain monitoring rather than full shape reconstruction (Xu and Sharif Khodaei, 2020). In contrast, quasi-distributed sensors based on Fibre Bragg Gratings (FBGs) have matured considerably over the past two decades and have been employed in numerous shape-sensing studies (Deaton et al., 2023; Jäckle et al., 2019; Roesthuis et al., 2014). Shape sensing using FBGs is achieved by integrating at least three grating arrays into either Multi-Core Fibres (MCF) or multi-fibre sensors composed of bonded single-mode fibres (Floris et al., 2021). Although MCFs offer compactness and extremely high measurement precision, their manufacturing complexity and high cost limit their suitability for large-scale deployment in geotechnical experiments and field applications (Roodsari et al., 2022).

To address these limitations, this study adopts a multi-fibre sensor configuration. The proposed design maintains a cross-sectional geometry similar to that of MCFs, while allowing a larger radial distance between the sensing fibres and the neutral axis, thereby enhancing bending sensitivity. A multi-fibre sensor incorporating four sensing nodes and twelve FBGs is assembled and experimentally evaluated. Shape reconstruction of a cantilever aluminium plate subjected to concentrated tip loading is carried out using two approaches. First, a conventional single-fibre algorithm is applied to assess planar bending behaviour. Second, a robust three-fibre algorithm is employed to capture more accurate and complex shape evolution. Comparisons with dial gauge measurements and theoretical solutions demonstrate the accuracy of the proposed methods and highlight their potential for application in geotechnical shape sensing.

2 METHODOLOGY

2.1 FBG measurement principles

Multi-fibre sensors capture structural shape through FBGs. Each grating is inscribed into an optical fibre core using ultraviolet laser radiation, creating a periodic modulation of the refractive index (Erdogan, 1997). As illustrated in Figure 1, an FBG functions as a wavelength-specific reflector when illuminated by broadband light. It reflects a narrowband wavelength, referred to as the Bragg wavelength (λ_B), while transmitting the remainder of the spectrum. The Bragg wavelength is defined as

$$\lambda_B = 2n_{eff}\Lambda \quad (1)$$

where n_{eff} is the effective refractive index of the fibre core, and Λ is the grating period.

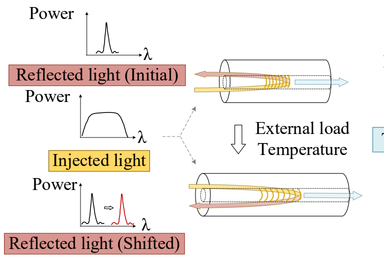

Figure 1. Schematic illustrating the operating principle of an FBG sensor.

Longitudinal strain (ε) and temperature variations (ΔT) induce a linear shift in the Bragg wavelength ($\Delta\lambda_B$), which can be expressed as

$$\Delta\lambda_B = \lambda_B[(1 - p_e)\varepsilon + (\alpha_\Lambda + \alpha_n)\Delta T)] \quad (2)$$

where p_e is the effective photo-elastic coefficient, and α_Λ and α_n are the thermal expansion and thermo-optic coefficients, respectively (Hill and Meltz, 1997). Under controlled laboratory environment, temperature variations were assumed to be negligible ($\Delta T \approx 0$). Consequently, the longitudinal strain can be directly obtained from the measured wavelength shift as

$$\varepsilon = \frac{1}{1 - p_e}\frac{\Delta\lambda_B}{\lambda_B} \quad (3)$$

For standard silica fibres, the effective photo-elastic coefficient is commonly taken as $p_e = 0.22$ (Hill and Meltz, 1997).

2.2 Shape reconstruction algorithms

Shape reconstruction is based on the geometric relationship between strain and curvature. Strain measurements obtained at discrete sensing nodes are first converted into curvature values. These curvatures are then interpolated and integrated along the sensor length to recover the continuous spatial shape.

Two shape reconstruction approaches are implemented and compared in this study: (i) a single-fibre method that assumes planar bending, and (ii) a multi-fibre method capable of reconstructing three-dimensional shape evolution.

2.2.1 Single-fibre reconstruction method

As a cost-effective and implementation-friendly approach for geotechnical model testing, a conventional single-fibre reconstruction algorithm is evaluated. It is applicable when the fibre is aligned with the principal bending plane and the distance between the fibre core and the neutral axis $\bar{y}$ is known.

Under the assumption of pure planar bending around the neutral axis, the curvature $\kappa(x)$ at a position x along the beam is linearly related to the measured longitudinal strain $\varepsilon(x)$ as

$$\kappa(x) = -\frac{\varepsilon(x)}{\bar{y}} \quad (4)$$

Assuming small deflections, the bending moment and corresponding curvature are expected to vary approximately linearly along the span (Kim and Cho, 2004). Accordingly, the curvature distribution is approximated by a linear regression fitted to the discrete sensing nodes:

$$\kappa(x) \approx \frac{d^2 v(x)}{dx^2} \approx A^* x + B^* (0 \leq x \leq L) \quad (5)$$

where $A^* = -A/\bar{y}$ and $B^* = -B/\bar{y}$ are regression coefficients derived from the measured strain data, and L is the total sensor length. By applying cantilever boundary conditions, zero deflection and zero rotation at the fixed end ($v(0) = 0$, $v'(0) = 0$), double integration of the curvature function yields the vertical deflection profile:

$$v(x) = \frac{1}{6} A x^3 + \frac{1}{2} B x^2 \ (0 \leq x \leq L) \quad (6)$$

This formulation provides a closed-form solution for reconstructing the deflection profiles using a single FBG array, making it suitable for bending-dominated geotechnical model tests.

2.2.2 Three-fibre reconstruction algorithm

To capture more complex deformation patterns, including three-dimensional bending and torsion, the analysis is extended to a multi-fibre sensor configuration. Each sensing segment is assumed to behave as a uniform and symmetric beam subjected to pure bending (Figure 2).

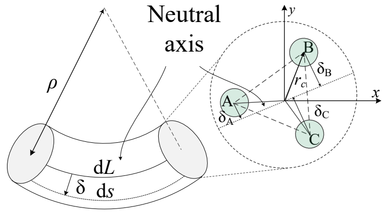

Figure 2. Deformation of the beam-assumed optic fibre section of length dL under pure bending conditions (the distances from the fibre centres to the neutral axis are δ_A, δ_B and δ_C).

For a fibre at a distance δ from the neutral axis with the arc length of ds, the longitudinal strain ε is related to the local curvature κ and bending radius ρ as

$$\varepsilon = \frac{ds - dL}{dL} = -\frac{\delta}{\rho} = -\kappa\delta \quad (7)$$

By measuring strains from three fibres within a cross-sectional segment, the curvature vector $\boldsymbol{\kappa_n}$ at each sensing node can be determined (Bronnikov et al., 2019; Roesthuis et al., 2014):

$$\boldsymbol{\kappa_n} = -\frac{2}{N r_c} \left(\sum_{i=1}^{N} \varepsilon_i cos\alpha_i \boldsymbol{n_x} + \sum_{i=1}^{N} \varepsilon_i sin\alpha_i \, \boldsymbol{n_y} \right) \quad (8)$$

$$\kappa_n = |\boldsymbol{\kappa_n}| \quad (9)$$

where $N = 3$ is the number of fibres, r_c is the radial distance from the centroid to each fibre, ε_i is the bending-induced strain measured by fibre i, and α_i is the angular position of fibre i relative to the local x-axis. The unit vectors $\boldsymbol{n_x}$ and $\boldsymbol{n_y}$ define the local coordinate system, as illustrated in Figure 2.

The discrete curvature vectors are interpolated along the sensor length to obtain continuous curvature $\kappa(s)$. The local curvature direction is defined as $\theta = angle(\kappa(s))$, and the torsion is calculated as $\tau(s) = \theta'(s)$. These quantities are integrated along the arc length using the Frenet–Serret frame to reconstruct the three-dimensional shape (Moore and Rogge, 2012):

$$\begin{bmatrix} \boldsymbol{T}'(s) \\ \boldsymbol{N}'(s) \\ \boldsymbol{B}'(s) \end{bmatrix} = \begin{bmatrix} 0 & \kappa(s) & 0 \\ -\kappa(s) & 0 & \tau(s) \\ 0 & -\tau(s) & 0 \end{bmatrix} \begin{bmatrix} \boldsymbol{T}(s) \\ \boldsymbol{N}(s) \\ \boldsymbol{B}(s) \end{bmatrix} \quad (10)$$

$$\boldsymbol{r}(s) = \int_0^L \boldsymbol{T}(s) ds + \boldsymbol{r}_0 \quad (11)$$

where $\boldsymbol{T}$, $\boldsymbol{N}$, and $\boldsymbol{B}$ are the tangent, normal, and binormal vectors, respectively; s is the arc length; and $\boldsymbol{r}_0$ is the initial position at the fixed base.

This procedure (Figure 3) enables accurate reconstruction of three-dimensional shape evolution from multi-fibre FBG measurements, allowing simultaneous detection of bending and torsion that cannot be resolved using a single-fibre algorithm.

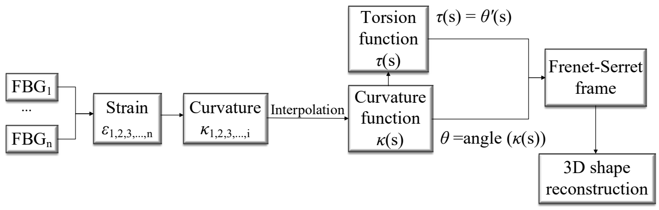

Figure 3. Workflow for shape reconstruction using an array of FBG sensors.

2.3 Experimental setup

2.3.1 Specimen and sensor configuration

The cantilever experiment was conducted using an aluminium plate with dimensions of $600\text{ mm} \times 35\text{ mm} \times 6.35\text{ mm}$ and a Young's modulus of 70 GPa. To facilitate sensor installation, two parallel grooves with a depth of 1 mm were machined along the longitudinal axis on the top surface of the plate, as shown in Figure 4. One end of the plate was rigidly clamped over a fixing length of 30 mm, thereby establishing a cantilever boundary condition for shape measurement.

The multi-fibre sensor employed in this study consists of three single-mode optical fibres arranged in an equilateral triangular configuration with an angular separation of 120°. To enhance mechanical durability, two fibres (bare diameter $\phi = 125\ \mu m$) were encased within protective silicone sleeves with an outer diameter of 2 mm, while the third fibre was left bare.

Each fibre contains four FBG sensing nodes with nominally uniform spacing. The measured centre-to-centre distances between adjacent nodes were 148 mm, 150 mm, and 149 mm, respectively, with each grating having a length of 18 mm. As shown in Figure 4, the first FBG sensing node (Node #1), corresponding to the lowest central Bragg wavelength, was positioned 60 mm from the fixed end. The remaining nodes were located at distances of 208 mm (Node #2), 358 mm (Node #3), and 507 mm (Node #4) from the fixed end. To prevent spectral overlap during wavelength-division multiplexing, the central Bragg wavelengths of the FBGs in Fibres A and B ranged from 1527 nm to 1557 nm, while those in Fibre C ranged from 1537 nm to 1567 nm. In both cases, a wavelength separation of 10 nm was maintained between adjacent gratings.

To assemble the multi-fibre sensor configuration, the three fibres were bonded to the aluminium plate using a high-modulus UV-curable adhesive to ensure rigid coupling and efficient strain transfer. The two silicone-sleeved fibres were embedded into the machined grooves on the top surface of the plate, while the third bare fibre was bonded directly to the underside of the plate. The lower fibre was centrally aligned between the two upper fibres along the longitudinal axis. This layout forms an approximately equilateral triangular arrangement across the plate thickness, with an angular separation of 120° and an effective radial distance of $r_c = 4.61$ mm from the neutral axis (Figure 4).

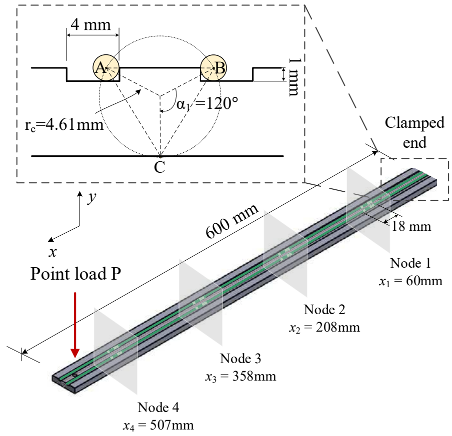

Figure 4. Geometry of the cantilever beam and layout of the multi-fibre shape sensing configuration.

2.3.2 Loading scheme and measurements

Stepwise point loads of 4 N, 7 N, 11 N, and 12 N were applied at a location 15 mm from the free end of the plate. The initial Bragg wavelength in the unloaded state is denoted as λ_0, and reflected wavelengths corresponding to the applied loads are denoted as $\lambda_4, \lambda_7, \lambda_{11}$, and λ_{12}, respectively.

For validation purposes, high-precision dial gauges were installed at longitudinal positions corresponding to the FBG sensing nodes to provide reference deflection measurements. In addition, analytical deflections calculated using classical cantilever beam theory are presented for comparison.

2.3.3 Interrogation and data processing

The optical sensing system was interrogated using a Luna Micron Optics HYPERION si255 8-channel interrogator, which provides real-time wavelength measurements for each fibre. The interrogator operates over a wavelength range of 1460-1620 nm, with a scan rate of 1000 Hz and a wavelength accuracy of 1 pm.

An Ethernet connection was used to link the interrogator to a computer, enabling data acquisition and transmission using ENLIGHT software, as shown in Figure 5. Subsequent data processing, including strain calculation and shape reconstruction, was performed using MATLAB.

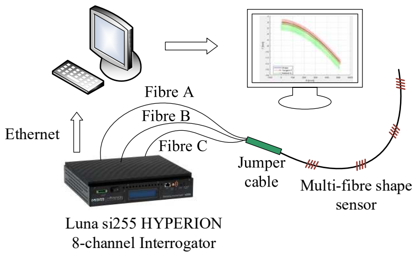

Figure 5. Interrogation and data acquisition scheme for the three-fibre FBG-based shape sensing system.

3 RESULTS AND DISCUSSION

3.1 Analysis of FBG measurements

Figure 6 shows the spectral evolution of the FBG sensors located on the tensile surface (Fibre A) and the compressive surface (Fibre C) under increasing applied loads. The wavelength shifts exhibit opposite directional trends, consistent with the fundamental bending mechanics of a cantilever beam. Fibre A shows a consistently positive wavelength shift ($\Delta\lambda > 0$), indicating tensile strain, whereas Fibre C exhibits a corresponding negative wavelength shift ($\Delta\lambda < 0$), confirming the presence of compressive stress.

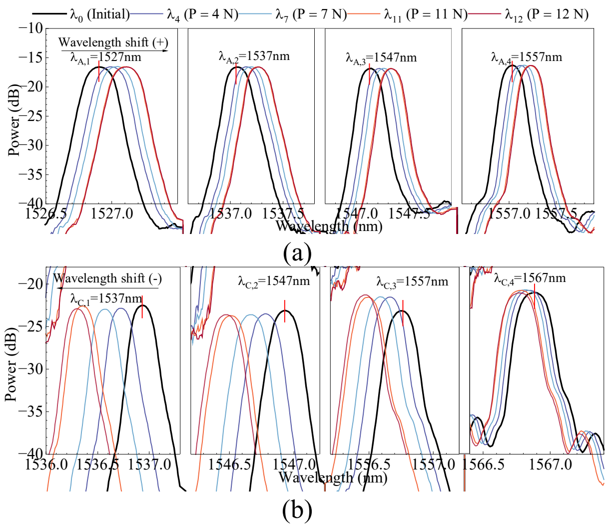

Figure 6. Evolution of reflected FBG spectra under applied loading for (a) Fibre A on the tensile surface; (b) Fibre C on the compressive surface.

For both fibres, the magnitude of the wavelength shift is strongly dependent on the longitudinal position. The sensing node closest to the clamped end (Node #1) exhibits the largest wavelength shift, with the response progressively decreasing towards the free end (Node #4). This spatial variation closely follows the theoretical bending moment distribution of a cantilever beam, in which surface strain is maximised at the fixed end and decreases approximately linearly along the span.

Notably, the bare fibre (Fibre C) exhibits a steeper wavelength shift-position gradient than the silicone-sleeved fibre (Fibre A). This behaviour is attributed to shear lag introduced by the compliant silicone sleeve, which partially attenuates strain transfer from the substrate to the fibre while preserving overall linearity.

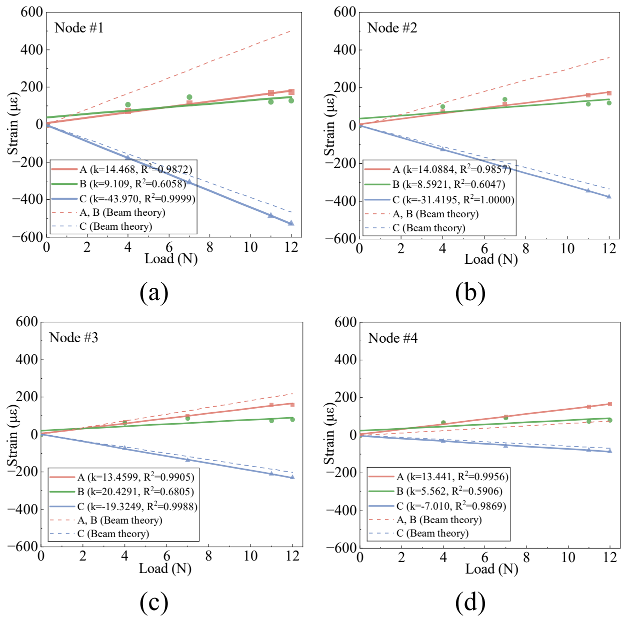

Figure 7. Strain-load response of the FBG sensors, illustrating linearity and sensitivity of 4 nodes: (a) Node #1; (b) Node #2; (c) Node #3; (d) Node #4.

Based on the measured wavelength shifts, longitudinal strains were calculated using Eq. (3), adopting an effective photo-elastic coefficient of $p_e = 0.22$. Figure 7 compares the measured strain response of all sensing nodes as a function of the applied load with the strain predictions based on Euler–Bernoulli beam theory. Linear regression analysis demonstrates that both the bare fibre (Fibre C) and one of the silicone-sleeved fibres (Fibre A) exhibit excellent linearity ($R^2 > 0.99$), indicating stable mechanical coupling and negligible hysteresis throughout the loading process. Fibre C remains in close agreement with the theoretical strain at all nodes, whereas Fibres A and B generally underestimate the strain but progressively approach the beam-theory prediction towards the free end. This trend reflects the reduction of constraint-induced local effects away from the clamped end, where the bending deformation more closely conforms to the assumptions of beam theory. At each sensing node, the bare fibre consistently exhibits a higher strain sensitivity than the silicone-sleeved fibres. This difference becomes increasingly obvious at the nodes towards the clamped end, where bending-induced strain is theoretically maximised in a cantilever beam. For example, at Node #1, the bare fibre exhibits a strain sensitivity of $-43.97\ \mu\varepsilon/N$, compared with $14.47\ \mu\varepsilon/N$ and $9.11\ \mu\varepsilon/N$ for the silicone-sleeved fibres. This reduction in sensitivity can be attributed not only to the shear lag effect discussed earlier, but also to imperfect adhesion between the fibre and its silicone sleeve, where slight relative sliding at the fibre-sleeve interface reduces effective strain transfer.

In contrast, Fibre B shows slightly reduced linearity compared with Fibre A. This behaviour is likely caused by local imperfections in the silicone sleeve, such as micro-voids or partial interfacial debonding, which can introduce variability in strain transfer and non-uniform shear lag under different load levels. Consequently, owing to its higher strain transfer efficiency and direct coupling to the substrate, data from bare fibre (Fibre C) were selected for subsequent conventional single-fibre shape reconstruction.

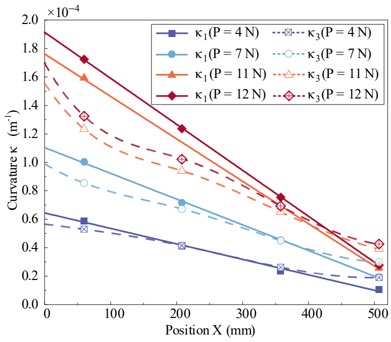

Figure 8. Curvature distributions obtained from the single-fibre and multi-fibre shape reconstruction methods.

Figure 8 compares the curvature distributions obtained from the single-fibre reconstruction (κ_1) and the multi-fibre reconstruction algorithm (κ_3). The single-fibre approach yields higher curvature values near the clamped end ($x = 60mm$), particularly at higher load levels. At the maximum load, the curvature estimated using the single-fibre method is approximately 30% higher than that obtained from the multi-fibre algorithm, while this discrepancy reduces to 11.3% at an applied load of 4 N. In addition, the curvature profile derived from the single-fibre method exhibits a steeper spatial gradient along the span. These discrepancies can be attributed to two primary factors. First, the single-fibre algorithm assumes an idealised neutral axis location. In practice, the presence of adhesive layers shifts the effective neutral axis, leading to curvature overestimation. Second, the surface-mounted bare fibre is more sensitive to localised stress concentrations near the clamped end, resulting in an amplified curvature gradient compared with the spatially averaged response captured by the multi-fibre configuration.

3.2 Shape reconstruction comparison and error analysis

Figure 9 compares the reconstructed deflection profiles obtained using the single-fibre and multi-fibre algorithms with ground-truth measurements from dial gauges and theoretical predictions based on cantilever beam theory.

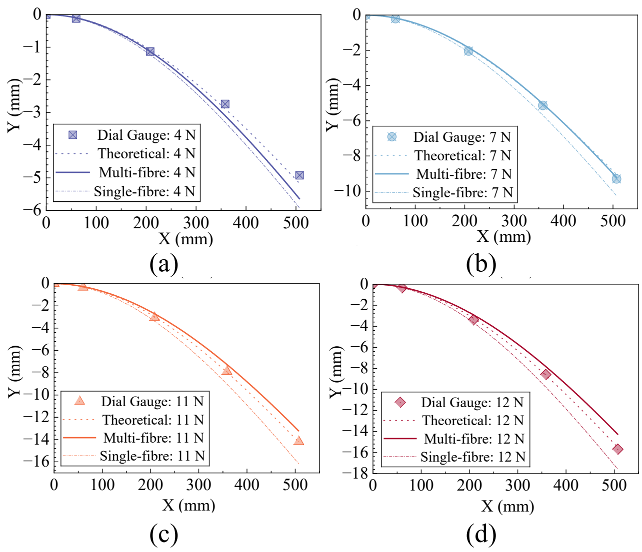

Figure 9. Comparisons of reconstructed deflection profiles with dial-gauge measurements and theoretical beam predictions for loads of (a) 4N; (b) 7N; (c) 11N; (d) 12N.

The single-fibre reconstruction consistently overestimates the deflection, particularly towards the free end of the beam. This behaviour arises from the integration-based reconstruction process, in which locally overestimated curvature values accumulate along the arc length, resulting in amplified end-point deviations. In contrast, the multi-fibre reconstruction closely follows the measured deflection profile along the entire span, demonstrating improved agreement with both experimental and theoretical references, despite slightly reduced curvature sensitivity. It is noted that imperfect fibre bonding and strain transfer associated with fibres encapsulated in compliant silicone sleeves may influence the reconstructed response. Under the current experimental setup, however, it is difficult to isolate the specific effects of the silicone-sleeved fibres.

The absolute shape error distribution is shown in Figure 10, and summary metrics, including maximum error per unit length and root-mean-square error (RMSE), are reported in Table 1. The absolute error δ_{abs} and relative error per unit length δ_{rel} are defined following Bronnikov et al. (2019) as:

$$\delta_{abs} = \|\boldsymbol{r}_i(s) - \boldsymbol{r}_{ref}(s)\|, \delta_{rel} = \delta_{abs}(s)/s \quad (12)$$

where $\boldsymbol{r}_i(s)$ is the reconstructed position vector, $\boldsymbol{r}_{ref}(s)$ represents the reference position, and s denotes the arc length.

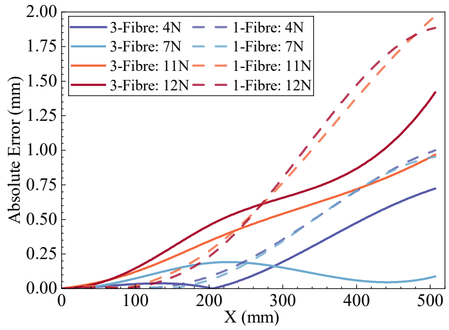

Figure 10. Distribution of absolute shape reconstruction error along the cantilever length.

Table 1. Summary of shape reconstruction errors.

Load Case	Max. Abs. Error δ_{abs} (mm)		Max. Abs. Error per length δ_{rel} (%)		RMSE (mm)	
Fibre #	1	3	1	3	1	3
4	1.000	0.723	0.197	0.143	0.477	0.324
7	0.954	0.192	0.188	0.038	0.470	0.116
11	1.972	0.969	0.389	0.191	0.949	0.528
12	1.884	1.420	0.372	0.280	0.976	0.678

As expected for integration-based algorithms, errors accumulate progressively along the arc length towards the free end. Under the maximum applied load of 12 N, the single-fibre method exhibits pronounced integration error, with an absolute tip error of 1.88 mm and a maximum relative error of 0.372%, whereas the three-fibre reconstruction reduces these values to 1.42 mm and 0.28%, respectively.

Optimal performance occurs at an intermediate load of 7 N, where the relative errors decrease to 0.188% and 0.038% for the single-fibre and multi-fibre methods, respectively. The load-dependent nature of the error is evident. At higher loads, increased curvature gradients lead to interpolation inaccuracies between sensing nodes, whereas at the low load of 4 N, relative errors are slightly elevated due to a reduced signal-to-noise ratio, which makes the reconstruction more sensitive to measurement noise.

This trend is further confirmed by the RMSE analysis. At the maximum load, the three-fibre algorithm achieves an RMSE of 0.678 mm, compared with 0.976 mm for the single-fibre method. At 7 N, the RMSE further decreases to 0.116 mm for the multi-fibre reconstruction, while the single-fibre approach remains at 0.470 mm, highlighting the superior accuracy of the multi-fibre method.

The improved performance of the multi-fibre approach can be attributed to three key factors:

1) Differential strain mechanism: Unlike single-fibre approaches that rely on absolute strain magnitudes, the vector-based multi-fibre algorithm derives curvature from relative strain differences between fibres. This effectively suppresses common-mode effects, such as temperature variations or uniform axial strain, thereby isolating the true bending-induced deformation.

2) Stable geometric baseline: The multi-fibre configuration benefits from a precisely defined core spacing (r_c), fixed by CNC machining, which provides a stable geometric reference. In contrast, the single-fibre method depends on the theoretical distance to the neutral axis ($\bar{y}$), which can be influenced by adhesive thickness and material inhomogeneity.

3) Spatial averaging and low-pass filtering: By combining measurements from multiple fibres, the multi-fibre algorithm inherently averages local strain fluctuations caused by stress concentrations, resulting in a smoother and more robust shape reconstruction.

Despite these improvements, minor discrepancies between the reconstructed and reference shapes remain, mainly due to manual assembly imperfections such as slight fibre misalignment, non-uniform adhesive layers, and potential axial offsets between FBG sensing nodes. In addition, uncertainties in the assumed photo-elastic coefficient may introduce small scaling errors. These systematic deviations could be further reduced in future work through calibration-based correction procedures.

4 CONCLUSIONS

This study experimentally validated two FBG-based shape sensing approaches for reconstructing the continuous shape of a cantilever plate, providing a practical framework for geotechnical model testing with different accuracy requirements. The single-fibre approach offers a cost-effective solution for scenarios dominated by principal-plane bending, where planar shape evolution is of primary interest. Although cumulative integration drift leads to larger deviations, its accuracy remains sufficient for in-plane shape sensing applications, such as pile bending tests. In contrast, the multi-fibre configuration demonstrated improved accuracy and robustness in shape reconstruction, attributable to its differential strain formulation and deterministic geometric baseline. Although under the current experimental conditions, fibre bonding and strain transfer through the silicone sleeve may blur the reconstructed response, the multi-fibre framework nonetheless provides a more stable basis for curvature reconstruction and is inherently extensible to more complex three-dimensional shape sensing.

The results further clarify the relationship between sensor configuration and shape-sensing dimensionality. A single fibre provides scalar information on curvature magnitude, two fibres enable resolution of in-plane bending direction and planar shape, and three fibres allow full three-dimensional shape reconstruction by determining the curvature vector and inferring torsion. This hierarchy establishes a systematic basis for designing fibre-optic shape sensing systems for geotechnical applications.

Future work will focus on calibration to mitigate systematic errors and on extending the proposed methods to more complex three-dimensional shape sensing. By enabling accurate and real-time shape measurement, the proposed approach provides a valuable tool for advancing soil-structure interaction research and scaled geotechnical model testing.

ACKNOWLEDGEMENTS

The authors acknowledge support from the Manchester-Melbourne-Toronto Research Fund.

REFERENCES

Barrias, A., Casas, J. R. and Villalba, S. (2016). A review of distributed optical fiber sensors for civil engineering applications. *Sensors*, *16*(5), 748. https://doi.org/10.3390/s16050748

Bronnikov, K., Wolf, A., Yakushin, S., Dostovalov, A., Egorova, O., Zhuravlev, S., Semjonov, S., Wabnitz, S. and Babin, S. (2019). Durable shape sensor based on FBG array inscribed in polyimide-coated multicore optical fiber. *Optics Express*, *27*(26), 38421-38434. https://doi.org/10.1364/OE.380816

Deaton, N. J., Sheft, M. and Desai, J. P. (2023). Towards FBG-based shape sensing and sensor drift for a steerable needle. *IEEE/ASME Transactions on Mechatronics*, *28*(6), 3041-3052. https://doi.org/10.1109/TMECH.2023.3239750

Di Sante, R. (2015). Fibre optic sensors for structural health monitoring of aircraft composite structures: Recent advances and applications. *Sensors*, *15*(8), 18666-18713. https://doi.org/10.3390/s150818666

Erdogan, T. (1997). Fiber grating spectra. *Journal of Lightwave Technology*, *15*(8), 1277-1294. https://doi.org/10.1109/50.618322

Floris, I., Adam, J. M., Calderón, P. A. and Sales, S. (2021). Fiber optic shape sensors: A comprehensive review. *Optics and Lasers in Engineering*, *139*, 106508. https://doi.org/10.1016/j.optlaseng.2020.106508

Hill, K. O. and Meltz, G. (1997). Fiber Bragg grating technology fundamentals and overview. *Journal of Lightwave Technology*, *15*(8), 1263-1276. https://doi.org/10.1109/50.618320

Jäckle, S., Eixmann, T., Schulz-Hildebrandt, H., Hüttmann, G. and Pätz, T. (2019). Fiber optical shape sensing of flexible instruments for endovascular navigation. *International Journal of Computer Assisted Radiology and Surgery*, *14*(12), 2137-2145. https://doi.org/10.1007/s11548-019-02059-0

Kim, N. S. and Cho, N. S. (2004). Estimating deflection of a simple beam model using fiber optic Bragg-grating sensors. *Experimental Mechanics*, *44*(4), 433-439. https://doi.org/10.1007/BF02428097

Moore, J. P. and Rogge, M. D. (2012). Shape sensing using multi-core fiber optic cable and parametric curve solutions. *Optics Express*, *20*(3), 2967-2973. https://doi.org/10.1364/OE.20.002967

Raffel, M., Willert, C., Scarano, F., Kähler, C. J., Wereley, S. and Kompenhans, J. (2018). *Particle Image Velocimetry: A Practical Guide*, 3rd ed., Springer. Cham, Switz. https://doi.org/10.1007/978-3-319-68852-7

Roesthuis, R. J., Kemp, M., van den Dobbelsteen, J. J. and Misra, S. (2014). Three-dimensional needle shape reconstruction using an array of fiber Bragg grating sensors. *IEEE/ASME Transactions on Mechatronics*, *19*(4), 1115-1126. https://doi.org/10.1109/TMECH.2013.2269836

Roodsari, S. M., Freund, S., Zam, A., Rauter, G. and Cattin, P. C. (2022). Fabrication and Characterization of a Flexible FBG-Based Shape Sensor Using Single-Mode Fibers. *IEEE Transactions on Biomedical Engineering*, *69*(8), 2488-2498. https://doi.org/10.1109/TBME.2022.3148040

Stanier, S. A., Blaber, J., Take, W. A. and White, D. J. (2016). Improved image-based deformation measurement for geotechnical applications. *Canadian Geotechnical Journal*, *53*(5), 727-739. https://doi.org/10.1139/cgj-2015-0253

White, D. J., Take, W. A. and Bolton, M. D. (2003). Soil deformation measurement using particle image velocimetry (PIV) and photogrammetry. *Géotechnique*, *53*(7), 619-631. https://doi.org/10.1680/geot.2003.53.7.619

Wood, D. M. (2017). *Geotechnical Modelling*. CRC Press. London, UK. https://doi.org/10.1201/9781315273556

Xu, C. and Sharif Khodaei, Z. (2020). Shape sensing with rayleigh backscattering fibre optic sensor. *Sensors*, *20*(14), 4040. https://doi.org/10.3390/s20144040

Zhang, C., Zhu, H., Chen, D., Xu, X., Shi, B. and Chen, X. (2019). Feasibility study of anchored fiber-optic strain-sensing arrays for monitoring soil deformation beneath model foundation. *Geotechnical Testing Journal*, *42*(4), 966-984. https://doi.org/10.1520/gtj20170321